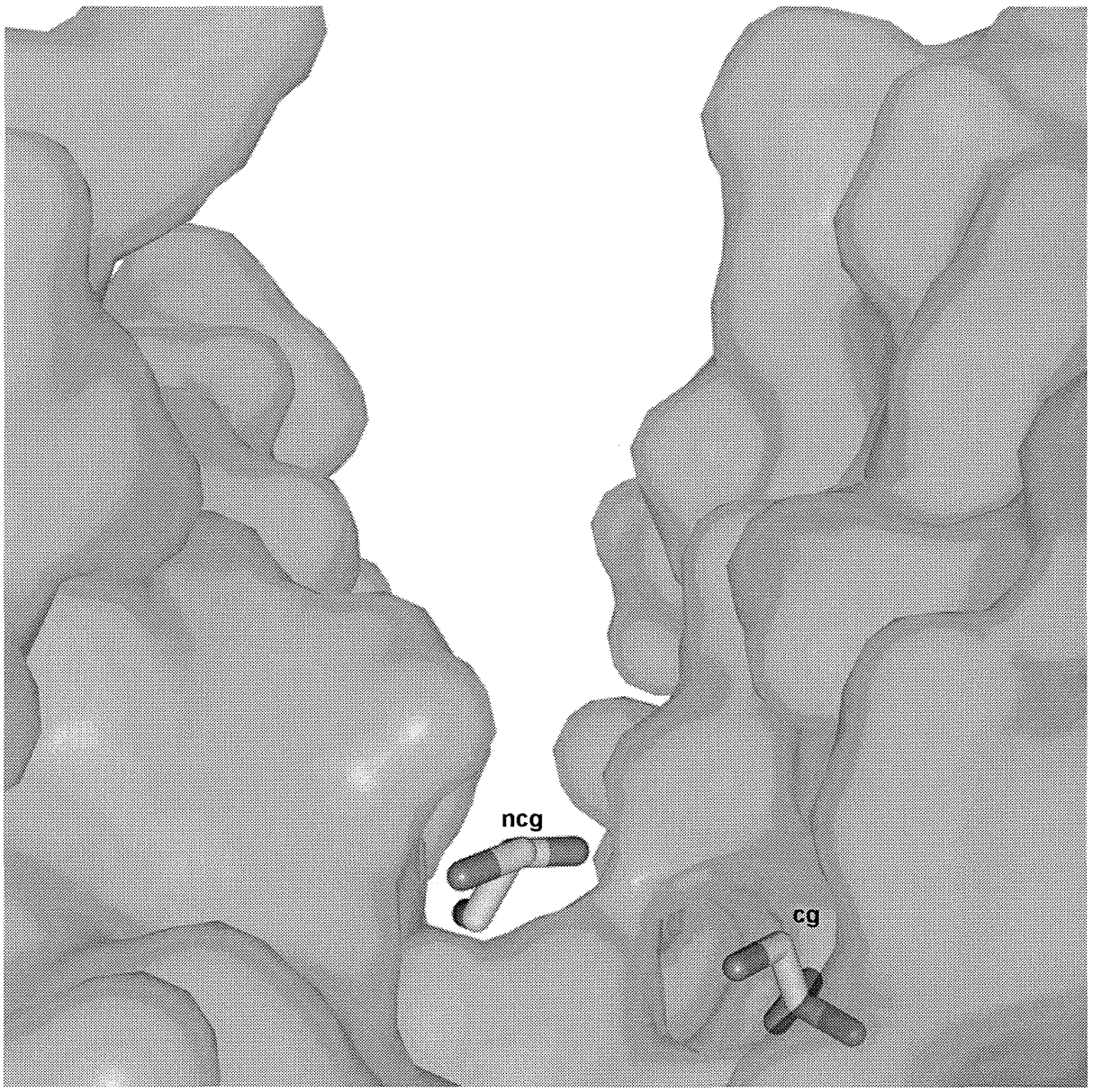

Figure S6

Table S1: Hydrogen bonded atoms at the dimer interphase of TbgGK

Source atoms (A-chain)	Residue location	Target atoms (B-chain)	Residue location	Distance Å
Thr382 / O	$(\beta15/\alpha14)^{A}$	Trp326 / Nε1	$\alpha12^{B}$	2.79
Leu380 / O	$(\beta15/\alpha14)^{A}$	Asn330 / Nδ2	$\alpha12^{B}$	2.95
Arg384 / N	$\alpha14^{A}$	Asn330 / O	$\alpha12^{B}$	2.76
Asn332 / O	$\alpha12^{A}$	Asn332 / Nδ2	$\alpha12^{B}$	2.97
Asn332 / Nδ2	$\alpha12^{A}$	Asn332 / Nδ2	$\alpha12^{B}$	3.28
		Asn332 / O	$\alpha12^{B}$	3.12
Trp509 / Nε1	CTL	Gly352 / O	$(\alpha13/\beta14)^{B}$	3.11
Met378 / O	$(\beta15/\alpha14)^{A}$	Gly373 / N	$(\beta14/\beta15)^{B}$	2.78
Met378 / N	$\beta15^{A}$	Gly373 / O	$(\beta14/\beta15)^{B}$	3.20
Ile375 / O	$\beta15^{A}$	Ile375 / N	$\beta15^{B}$	2.95
Ile375 / N	$\beta15^{A}$	Ile375 / O	$\beta15^{B}$	2.87
Gly373 / O	$(\beta14/\beta15)^{A}$	Met378 / N	$\beta15^{B}$	2.94
Gly373 / N	$(\beta14/\beta15)^{A}$	Met378 / O	$\beta15^{B}$	3.13
Asn330 / Nδ2	$\alpha12^{A}$	Leu380 / O	$(\beta15/\alpha14)^{B}$	2.98
Trp326 / Nε1	$\alpha12^{A}$	Thr382 / O	$(\beta15/\alpha14)^{B}$	2.85
Asn330 / Nδ2	$\alpha12^{A}$	Thr382 / O	$(\beta15/\alpha14)^{B}$	3.16
Asn330 / O	$\alpha12^{A}$	Arg384 / N	$\alpha14^{B}$	2.88
Lys508 / O	CTL	Arg506 / Nη1	$\alpha18^{B}$	2.63
Lys508 / O	CTL	Arg506 / Nη2	$\alpha18^{B}$	2.99
Arg506 / Nε	$\alpha18^{A}$	Lys508 / O	CTL	3.30
Arg506 / Nη2	$\alpha18^{A}$	Lys508 / O	CTL	2.64
Gly352 / O	$(\alpha13/\beta14)^{A}$	Trp509 / Nε1	$(\alpha13/\beta14)^{B}$	3.04

Parentheses represent loops between the indicated secondary structures

Superscripts indicate the chain in which residues are located

CTL means C-terminal loop

Table S2: Interactions between TbgGK, G3P, and ADP

Interacting atoms in substrates		Interacting atoms in TbgGK		Distance Å	Interaction
G3P (Phosphate donour substrate)					
Carbon	C1	Trp104	ring Cs	3.80	Stacking interaction
	C2	Phe279	ring Cε, Cζ	3.80	Stacking interaction
	C3	Trp104	ring Cs	3.60	Stacking interaction
Hydroxyl	O1	Arg84	Nε	3.08	Hydrogen bond
	O1	Arg84	Nη2	3.01	Hydrogen bond
	O1	Glu85	Oε1	2.99	Hydrogen bond
	O2	Asp254	Oδ2	2.40	Hydrogen bond
Phosphate	O1P	Gln255	Nε2	3.28	Hydrogen bond
	O2P	Thr276	O	3.04	Hydrogen bond
	O2P	Thr11	Oγ1	2.81	Hydrogen bond
	O2P	Thr276	Oγ1	3.14	Hydrogen bond
	O3P	Asp254	Oδ1	3.25	Hydrogen bond
	O3P	Thr11	Oγ1	3.03	Hydrogen bond
Active site ADP (Phosphate acceptor substrate)					
Adenine	N6	Gln255	Nε2	3.08	Hydrogen bond
	C2	Thr273	Cγ2	3.89	Hydrophobic interaction
	C8	Thr276	Cβ	3.53	Hydrophobic interaction
	C8	Thr276	Cα	3.99	Hydrophobic interaction
Ribose	C2	Gly275	Cα	3.89	Hydrophobic interaction
Phosphate	O2B	Thr12	Oγ1	3.19	Hydrogen bond
	O3B	Thr12	Oγ1	3.25	Hydrogen bond
	O3B	Thr12	N	3.03	Hydrogen bond

Table S3: Interactions between TbgGK and glycerol

Interacting atoms in substrates		Interacting atoms in TbgGK		Distance Å	Interaction
Catalytic glycerol (Phosphate acceptor substrate)					
Carbon	C1	Phe279	ring Cε, Cζ, Cδ	3.74	Stacking interaction
	C3	Trp104	ring Cε, Cζ	3.80	Stacking interaction
Hydroxyl	O2	Arg84	N	2.87	Hydrogen bond
	O2	Asp254	Oδ1	2.87	Hydrogen bond
	O2	Asp254	Oδ2	2.67	Hydrogen bond
	O3	Arg84	Nη2	2.73	Hydrogen bond
	O3	Glu85	Oε1	3.19	Hydrogen bond
Non-catalytic glycerol					
Hydroxyl	O3	Thr276	N	3.15	Hydrogen bond
	C1	Gly275	Cα	3.70	Hydrophobic Interaction
	C1	Gly277	Cα	3.58	Hydrophobic Interaction
	C2	Thr276	Cβ	3.51	Hydrophobic Interaction

Table S4: Interactions between TbgGK and second site ADP

Interacting atoms in substrates			Interacting atoms in TbgGK		Distance	
Interaction						
					Å	
Second site ADP^{A} (unknown function)						
Adenine	Ring C4, 5, 6, & 8		Arg477	Cδ & Cζ	3.60	Stacking interaction
	N3		Glu478	Oε2	3.16	Hydrogen bond
Ribose	O4′		Arg477	Nε	3.30	Hydrogen bond
Phosphate	O2A		Arg22	Nη1	2.63	Hydrogen bond
	O2A		Glu478	Oε1	2.49	Hydrogen bond
	O1B		Arg24	Nη1	2.73	Hydrogen bond
	O2B		Arg22	Nη1	2.99	Hydrogen bond
	O2B		Arg24	Nη2	3.14	Hydrogen bond
	O1A	ADP^{B}		N6	3.27	Hydrogen bond
	O2B	ADP^{B}		O2B	2.94	Hydrogen bond
	O2B	Mg^{2+}			2.15	Coordinate bond
Second site ADP^{B} (unknown function)						
Adenine	Ring C5, 6, 8		Arg22	Cδ & Cζ	3.80	Stacking interaction
	C2		Met1	Cε	3.43	Hydrophobic interaction
	N7		Arg22	Nη1	3.30	Hydrogen bond
	N7		Arg22	Nη1	3.35	Hydrogen bond
	N6	ADP^{A}		O1A	3.27	Hydrogen bond
Ribose	O2′		Asp20	Oδ2	2.90	Hydrogen bond
	O3′		Tyr3	OH	3.00	Hydrogen bond
	C2′		Val26	Cγ1	3.70	Hydrophobic interaction
	C3′		Val26	Cγ1	3.70	Hydrophobic interaction
	C3′		Val26	Cβ1	3.94	Hydrophobic interaction
Phosphate	O2B		Arg22	Nη1	2.66	Hydrogen bond
	O3B		Arg24	Nη2	2.93	Hydrogen bond
	O2B	ADP^{A}		O2B	2.94	Hydrogen bond
	O2B	Mg^{2+}			2.05	Coordinate bond

Table S5: Sequences of primers used for creating mutants of TbgGK with single amino-acid substitutions

Mutant	Primer sequence (sense/antisense; 5′ to 3′)
M1A	GGGAATTGATCCCTTCACCGCGAAGTACGTCGGATCCATT
	AATGGATCCGACGTACTTCGCGGTGAAGGGATCAATTCCC
Y3F	AATTGATCCCTTCACCATGAAGTTCGTCGGATCCAT
	ATGGATCCGACGAACTTCATGGTGAAGGGATCAATT
T11V	GATCCATTGACCAGGGAGTAACCAGCACCCGCTTCA
	TGAAGCGGGTGCTGGTTACTCCCTGGTCAATGGATC
T12V	CCATTGACCAGGGAACAGTCAGCACCCGCTTCATCA
	TGATGAAGCGGGTGCTGACTGTTCCCTGGTCAATGG
D20A	CTTCATCATCTTCGCTGAGCGGCAGCGCC
	GGCGCTGCCGCTCAGCGAAGATGATGAAG
R22A	CATCTTCGATGAGGCGCAGCGCCCCGTC
	GACGGGGCGCTGCGCCTCATCGAAGATG
R24A	CGATGAGCGGCAGGCCCCCGTCTCGGTG
	CACCGAGACGGGGGCCTGCCGCTCATCG
T273V	GGTGAGGCCAAGAACGTATACGGCACCGGCTG
	CAGCCGGTGCCGTATACGTTCTTGGCCTCACC
T276V	CCAAGAACACATACGGCGTCGGCTGCTTCCTGTTGA
	TCAACAGGAAGCAGCCGACGCCGTATGTGTTCTTGG
R477A	AAGGCCGTGTCGCGAGCCGAGAATTCGTGG
	CCACGAATTCTCGGCTCGCGACACGGCCTT
E478A	CGTGTCGCGACGCGCGAATTCGTGGAAGA
	TCTTCCACGAATTCGCGCGTCGCGACACG

Cancer Science
Japanese Cancer Association JCA
Open Access

Newly defined aberrant crypt foci as a marker for dysplasia in the rat colon

Masako Ochiai,[1] Yoshitaka Hippo,[1] Masashi Izumiya,[2] Masatoshi Watanabe[3] and Hitoshi Nakagama[1]

[1]Division of Cancer Development System, National Cancer Center Research Institute, Tokyo; [2]Department of Gastroenterology, Graduate School of Medicine, The University of Tokyo, Tokyo; [3]Division of Materials Science and Chemical Engineering, Graduate School of Engineering, Yokohama National University, Yokohama, Japan

Key words
Aberrant crypt foci, azoxymethane, colon cancer, dysplasia, rat

Correspondence
Yoshitaka Hippo, Division of Cancer Development System, National Cancer Center Research Institute, 5-1-1 Tsukiji, Chuo-ku, Tokyo 104-0045, Japan.
Tel: +81-3-3547-5201; Fax: +81-3-3542-2530;
E-mail: yhippo@ncc.go.jp

Funding Information
Ministry of Health, Labor and Welfare of Japan; Japan Society for the Promotion of Science.

Received January 3, 2014; Revised May 6, 2014; Accepted May 9, 2014

Cancer Sci **105** (2014) 943–950

doi: 10.1111/cas.12446

Dysplasia represents a preneoplastic status in multistep colon carcinogenesis. Whereas laborious preparation of thin sections is required for its diagnosis, we here show that newly defined aberrant crypt foci (ACF) simply mark the majority of the dysplasia on the whole colon. Specifically, decoloring of the azoxymethane-treated rat colon after scoring classical ACF (cACF) resulted in visualization of a subset of aberrant crypts that remained densely stained. They were morphologically classified into three subtypes, of which two with compressed luminal openings proved highly correlated with dysplasia. Accordingly, we designated those foci harboring either of the two crypt subtypes as dysplasia-associated ACF (dACF). By serially applying different detection methods for known preneoplastic lesions to the same colon, we showed that most dACF had already been identified as cACF, and a few newly identified dACF contained an entire population of more advanced lesions, such as flat ACF and mucin-depleted foci. Consequently, integrative scoring of cACF and dACF enabled capture of all early lesions of the colon. Furthermore, 94% of the dACF showed dysplasia and 90% of the dysplastic lesions proved to be dACF. Thus, dACF is a promising marker for dysplasia, likely facilitating precise identification of the early stages of colon carcinogenesis.

Step-wise accumulation of genetic events underlies histological transition in colon carcinogenesis.[1–4] Aberrant crypt foci (ACF), clusters of enlarged thick crypts visualized by methylene blue (MB) staining, can be easily detected under a microscope at low magnification, and are the earliest identifiable lesions.[5,6] As their incidence at an early time point is highly correlated with eventual tumor incidence,[7] they have been widely used in evaluating carcinogenicity of chemicals.[8] However, their specificity as tumor precursors has been questioned, partly due to their predominant location in the proximal colon, where tumors do not develop, and gradual disappearance over time.[9,10] Moreover, ACF frequently harbor mutations in *Kras*, but rarely in adenomatous polyposis coli (*Apc*).[11–13] These findings strongly suggested that the majority of ACF might not be true preneoplastic lesions. Frequent *Apc* inactivation and β-catenin accumulation strongly suggest that dysplastic ACF[4,14–16] or crypts with β-catenin accumulation[17–19] might be specific tumor precursors, but they need histological analysis to be identified.

There are other non-ACF lesions on the whole colon. Flat dysplastic ACF (fACF) are less densely stained foci by brief exposure to MB.[10] Flat dysplastic ACF are likely associated with *Apc* inactivation, as $Apc^{min/+}$ mice spontaneously develop equivalent lesions, but not classical ACF (cACF).[20] Mucin-depleted foci (MDF) are the stain-defect lesions by periodic acid–Schiff (PAS), which readily detects mucin.[9,21] Unlike cACF, these two lesions develop predominantly in the distal colon and exhibit high-grade dysplasia. Moreover, chronological analysis has indicated that foci are likely tumor precursors.[9,10] However, they manifest only a low sensitivity for dysplasia.

Feeding rats with a dietary mutagen, 2-amino-1-methyl-6-phenylimidazo[4,5-*b*]pyridine (PhIP), allows recapitulation of colon carcinogenesis, providing many insights into the molecular mechanisms.[14,22–28] While characterizing PhIP-induced ACF, we noted that addition of a decoloring step could result in selective visualization of some stained foci. These foci tended to be more dysplastic than classical ACF, and the higher staining intensity of the foci could considerably, if not always, predict a higher likelihood of being dysplastic.[29] These findings raised the possibility that dysplasia could be identified as a new type of ACF. In this study, we verified this notion, and showed that the new ACF might be reasonably useful to evaluate the early stages of colon carcinogenesis.

Materials and Methods

Animal studies. Five-week-old F344 male rats were purchased from Clea Japan (Tokyo, Japan). The rats were s.c. treated with azoxymethane (AOM; Nard Institute, Osaka, Japan) at a dose of 15 mg/kg twice at the age of 6 and 7 weeks, and killed 9 weeks after the last treatment. The institutional committee for ethics in animal experimentation approved the protocol for animal experiments. The experiments were carried out in accordance with the guidelines for

animal experiments of the National Cancer Center (Tokyo, Japan).

Identification of cACF and dACF. The formalin-fixed colons were stained with 0.2% MB in PBS for 20 min, and the number of cACF[5] was counted. The colons were further stained with 0.2% MB for 20 min, and soaked in 70% methanol for 6 min for destaining.[29] Stained crypts were classified into three subtypes: crypts larger than surrounding normal ones with proportionally large and narrow openings were designated as *c*-type and *cd*-type, respectively, and crypts smaller than surrounding normal ones with narrower openings were designated as *d*-type. These three subtypes were readily distinguishable under a microscope, but objective evaluation was also carried out. The external diameter of normal (R_N) and aberrant crypts (R), and the internal diameter of aberrant crypts (*r*) were measured on captured images to calculate relative luminal opening size and relative crypt size. Foci containing at least a single crypt of either *cd*-type or *d*-type crypts were diagnosed as dysplasia-associated ACF (dACF). The signal intensity ratio (SIR) of the foci was determined as previously described.[29]

Serial scoring of preneoplastic lesions in a whole mounted colon. The formalin-fixed colons were divided into four segments, which were subject to serial different staining. The mucosal surface was examined under an inverse light microscope, and pictures across the whole colon were taken at each step for later comparison of the images of the same foci. Fragments were first soaked in 1% Alcian blue (AB), pH 2.5, for 30 min, and subsequently in 0.2% MB for 5 s to detect MDF and fACF, respectively. We adopted the staining solely with AB for the detection of MDF,[21] instead of the original high iron diamine–AB staining,[9] to avoid interference of high iron diamine with MB in evaluating ACF. Subsequently, the number of cACF and dACF were counted.

Histological analysis. For vertical sections, the colons were cut into pieces 3 mm long and 6 mm wide, so that each dACF would be located in the center of the fragment. For horizontal sections, the colons were first cut longitudinally into two strips, and subsequently segmented laterally into 8-mm-long pieces. These pieces were embedded in paraffin and cross-sections were prepared in 4 μm. Serial sections were subject to H&E staining without prior knowledge of information on surface examination. Dysplastic lesions were further graded into three classes as previously described.[30] The AB-PAS staining was carried out for the detection of foci that had completely lost mucin, which we designated as mucin-depleted crypts (MDC). Crypts with an accumulation of β-catenin in the cytoplasm or nucleus were diagnosed as β-catenin accumulating crypts (BCAC).[19,29]

Mutation analysis. Genomic DNA was selectively collected from BCAC by microdissection from the unstained serial sections of 20 independent samples. Extracted DNA was sub-

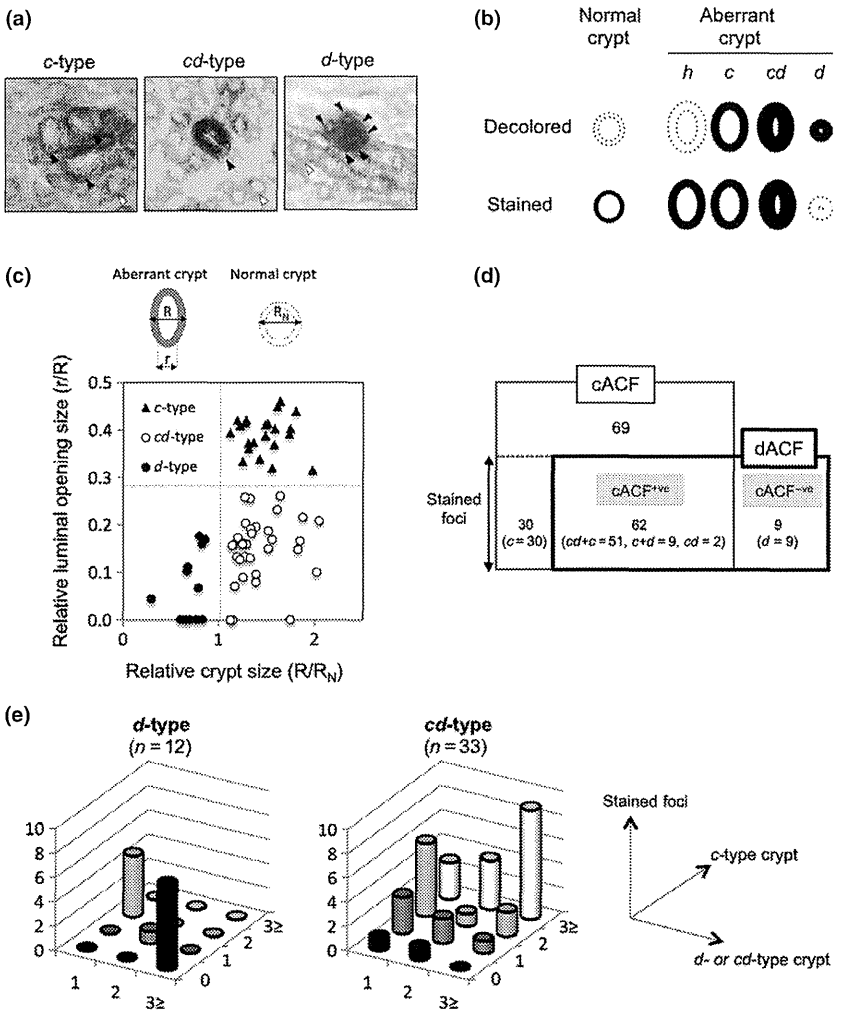

Fig. 1. Crypt-based characterization of azoxymethane-induced dysplasia-associated aberrant crypt foci (dACF). (a) Typical images of the three crypt subtypes (closed arrowheads) constituting dACF: c-type, enlarged crypt and broad opening; *cd*-type, enlarged crypt and narrow opening; and *d*-type, small crypt and narrow opening. Each arrowhead points to a single crypt. Note that normal crypts in surrounding mucosa (open arrowheads) could serve as a reference with a diameter of approximately 30 μm. (b) Schematic view of the crypt subtypes. A ring-shaped image represents the morphology of epithelial lining. Dashed lines indicate invisible status. (c) Classification of aberrant crypts by objective and subjective methods. Note that visual judgment and strict quantification gave completely concordant results for randomly selected crypts ($n = 66$). r, internal diameter of aberrant crypts; R, external diameter of aberrant crypts; R_N, external diameter of normal crypts. (d) Venn diagram for classical ACF (cACF) and dACF. Dysplasia-associated ACF (shaded box) was divided into two subgroups, $cACF^{+ve}$ and $cACF^{-ve}$, depending on the presence of overlap with cACF (open box). Composition of crypt subtype in stained foci is indicated in parenthesis. (e) Breakdown of crypt subtypes within stained foci. Each axis of the bar chart depicts the number of aberrant foci, c-type crypt and *d*- or *cd*-type crypt.

ject to amplification of exon 3 of the *Ctnnb1* gene by PCR, as previously described.[16] Polymerase chain reaction products were purified and directly sequenced by the standard Sanger method.

Results

Decoloring of MB-stained colon segregated three subtypes of aberrant crypts. We previously showed that more accurate detection of dysplasia might be achieved by destaining of cACF, although with laborious procedures, and found that the narrow opening might suggest the dysplastic nature of the foci.[29] We then hypothesized that stained foci harboring crypts with narrow opening, or dACF as tentatively designated, might be equivalent to dysplasia. To address this issue, we examined a rat colon treated with AOM. Starting with examining 161 induced cACF, we noted that decoloring gave rise to three morphologically distinct subtypes of stained crypts (Fig. 1a). We designated enlarged crypts with large openings, and small crypts with narrow openings as *c*-type and *d*-type, respectively, to emphasize specific features of cACF and dACF (Fig. 1B). Accordingly, enlarged crypts with narrow openings were designated as *cd*-type. Normal crypts and a subset of crypts within cACF turned invisible after decoloring. We designated the latter as *h*-type crypts (Fig. 1B), as such crypts constituted hyperplasia.[29] Thus, various types of crypts were differentially visualized through decoloring. We now redefined dACF as foci harboring at least single *d*- or *cd*-type crypt.

Dysplasia-associated ACF consisted of diverse combinations of crypt subtypes. The three crypt subtypes were morphologically so distinct that the right diagnosis could be made even by visual judgment. In fact, rigorous quantification of the size of both the crypt and its luminal openings for 66 randomly selected crypts gave completely concordant results (Fig. 1c). Direct comparison of the images of 71 dACF before and after

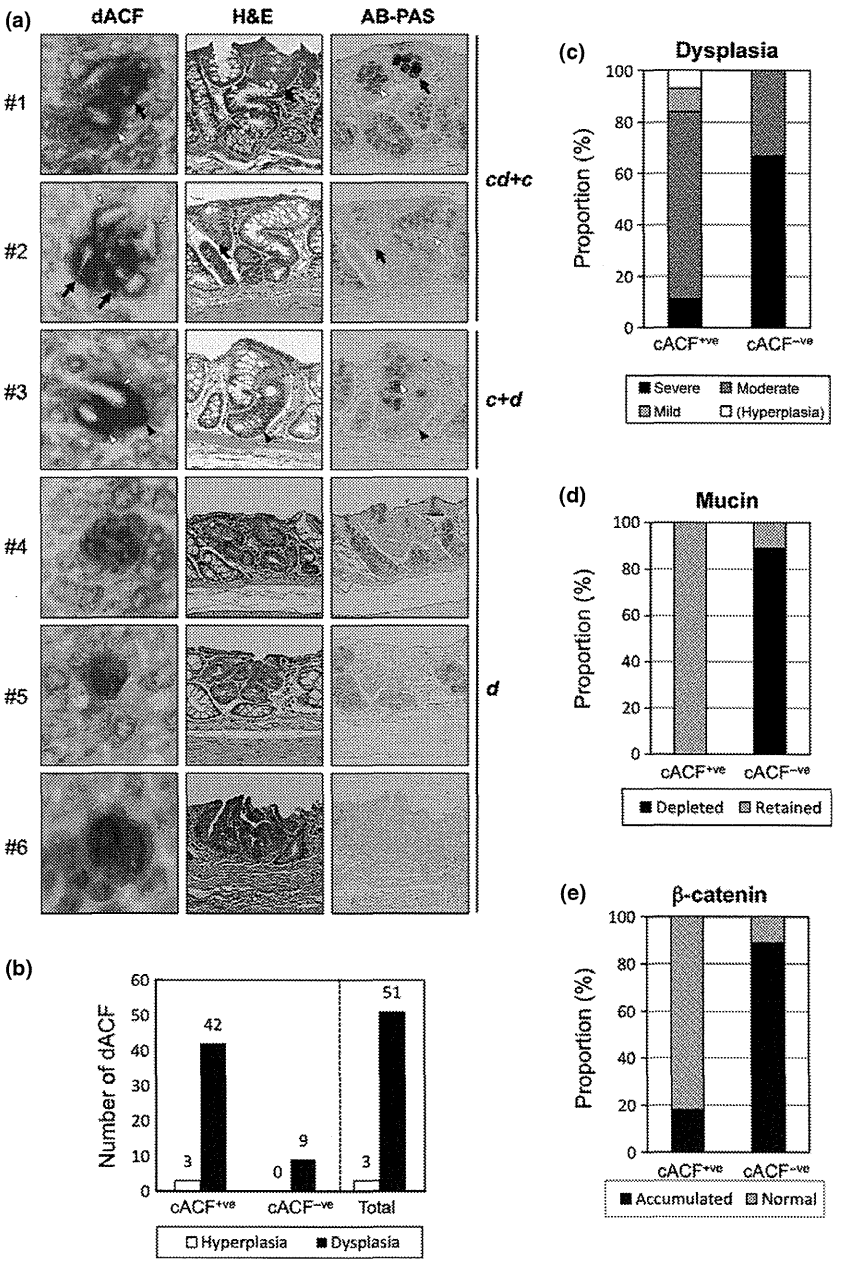

Fig. 2. Histological features of dysplasia-associated aberrant crypt foci (dACF). (a) Representative images of dACF (left panel) and corresponding histological features with H&E (middle panel) and Alcian blue–periodic acid–Schiff (AB-PAS) (right panel) staining. A single crypt of *c*-type (enlarged crypt and broad opening; open arrowheads), *cd*-type (enlarged crypt and narrow opening; arrow), and *d*-type (small crypt and narrow opening; closed arrowheads) is individually indicated for classical ACF (cACF)$^{+ve}$ (#1–3). Classical ACF^{-ve} consisted solely of *d*-type crypts (#4–6). Mucin expression was decreased in *cd*-type crypts (arrow) and completely depleted in *d*-type crypts (closed arrowheads). Accumulation of red granules indicative of Paneth cell differentiation (#4 and #5), consistent with severe dysplasia. (b–e) Comparison of cACF^{+ve} and cACF^{-ve}. The number of lesions with hyperplasia and dysplasia (b), and proportion of dysplastic lesions with each histological grade (c), with mucin depletion (d), and with β-catenin accumulation (e) are shown in the bar charts.

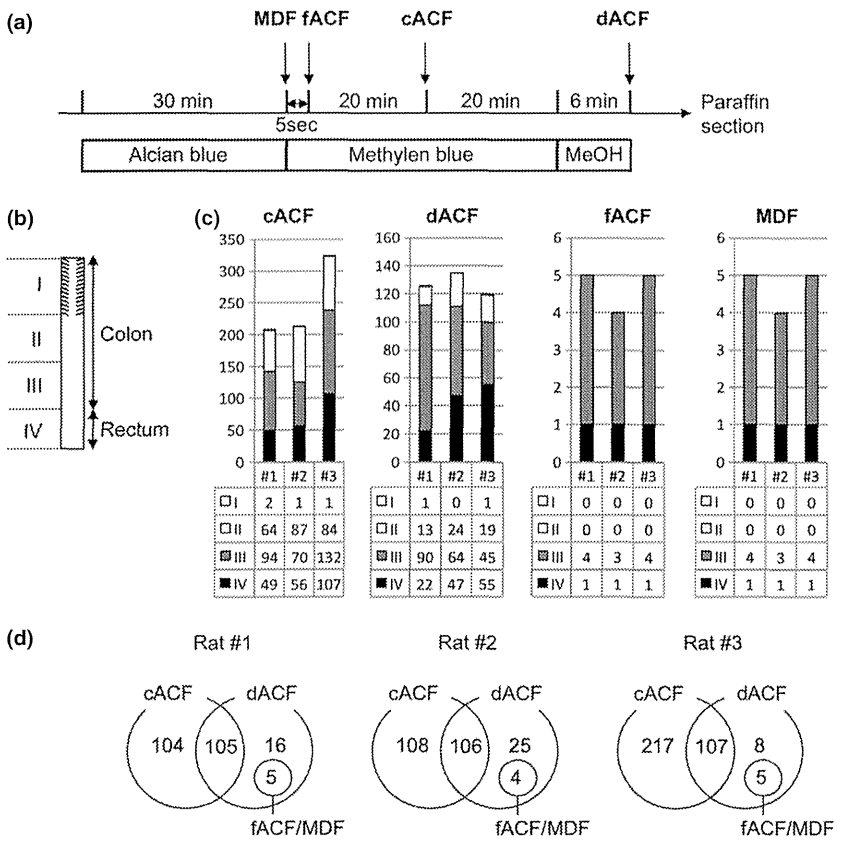

Fig. 3. Serial scoring of multiple preneoplastic lesions on the same colon. (a) A schematic diagram of the serial detection of multiple preneoplastic lesions. The images of mucosal surfaces were captured at the end of each step (arrows) for comparison at a later time point. (b) Colons were cut open longitudinally and separated into four segments (I–IV). (c) Bar chart showing the number of preneoplastic lesions per segment. #1–3 corresponds to the colons of three individual F344 male rats. Note that dysplasia-associated aberrant crypt foci (dACF), flat ACF (fACF), and mucin-depleted foci (MDF) are more enriched in segments III and IV compared to classical ACF (cACF). (d) Venn diagram for the number of cACF, dACF, and fACF/MDF for each rat.

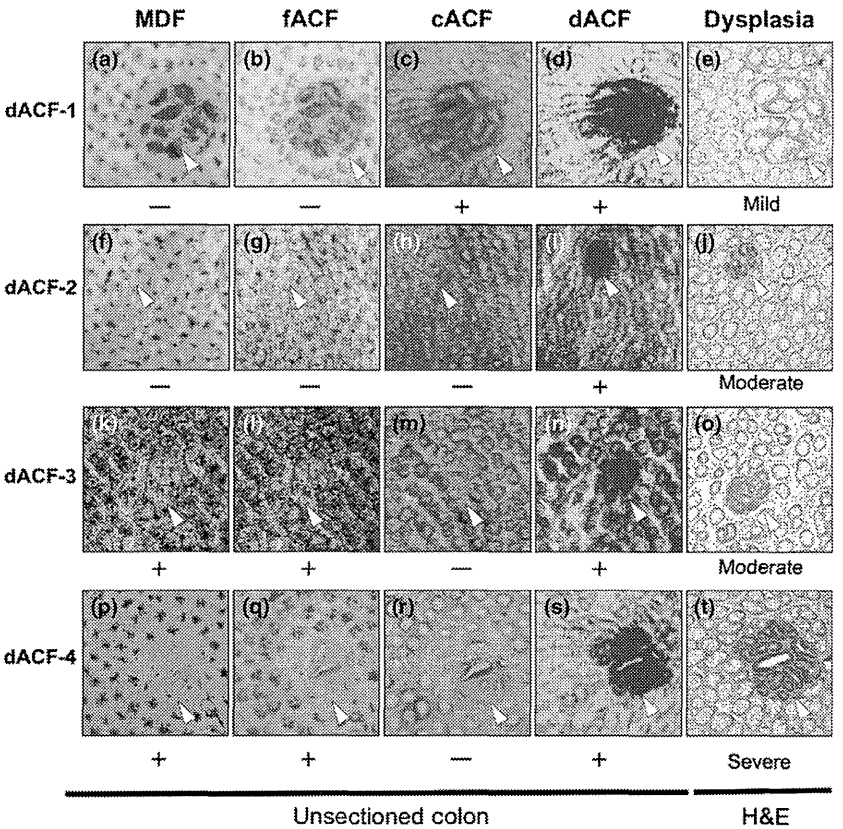

Fig. 4. Direct comparison between images of the same foci visualized by different methods: lesion dysplasia-associated aberrant crypt foci-1 (dACF-1) with mild dysplasia (a–e); lesions dACF-2 (f–j) and dACF-3 (k–o) with moderate dysplasia; and lesion dACF-4 with severe dysplasia (p–t). The left four columns show the images obtained by scoring preneoplastic lesions on the mucosal surface, and the diagnosis is indicated below the images as – (negative) or + (positive). The far right column depicts H&E staining of the corresponding lesions in horizontal sections, where the grade of dysplasia is shown below the images. Open arrowheads point to the area where the dysplastic lesions are supposed to be located in each image.

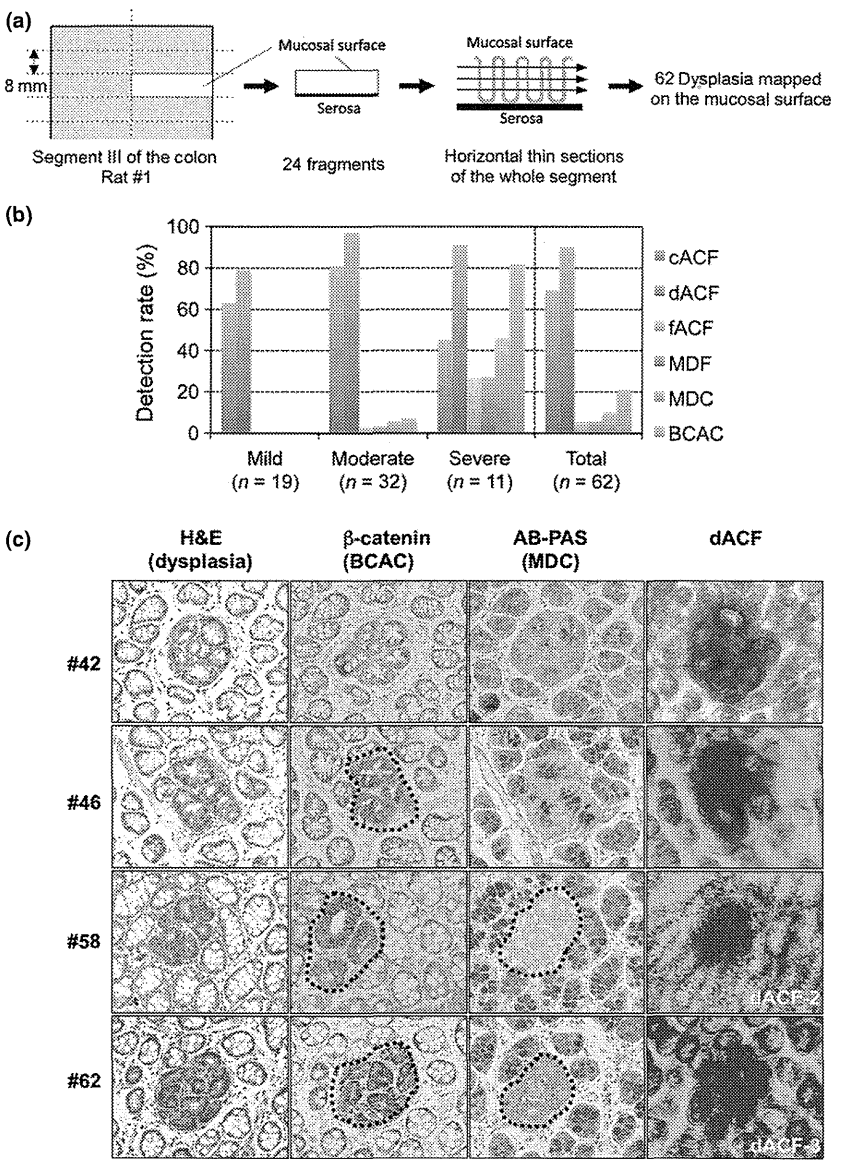

Fig. 5. Robust identification of dysplasia by scoring dysplasia-associated aberrant crypt foci (dACF). (a) Schematic diagram of the comprehensive histological analysis. A fixed colon from rat #1 was longitudinally cut open and segment III (shaded area) was divided into 24 fragments of 8 mm width (open rectangle) to cover the whole area by horizontal sections. (b) Successful detection rate of dysplasia for each preneoplastic lesion. Note that dACF provides the highest sensitivity in all grades of dysplasia. (c) Histological features of four representative dACF. Images of serial sections from the same lesion are shown. Dashed line circles β-catenin accumulating crypts (BCAC) or mucin-depleted crypts (MDC). Note that Paneth differentiation is evident in #58 and #62 (dACF-2 and -3 in Fig. 4, respectively), consistent with severe dysplasia. AB-PAS, Alcian blue–periodic acid–Schiff; cACF, classical ACF; fACF, flat ACF; MDF, mucin-depleted foci.

decolorization revealed that 62 and 9 had been diagnosed as $cACF^{+ve}$ and $cACF^{-ve}$, respectively (Fig. 1d). Nine newly identified $cACF^{-ve}$ consisted solely of *d*-type crypts, whereas 62 $cACF^{+ve}$ had various compositions of crypt subtypes. Most foci contained both *cd*- and *c*-type crypts (51/62), but some foci consisted of *cd*-type crypts alone (2/62), or with both *c*- and *d*-type crypts (9/62) (Figs 1d and 2a). Interestingly, *cd*- and *d*-type crypts never coexisted in the same foci, and the foci with more than two *d*-type crypts tended not to coexist with *c*-type crypts, which was not the case with *c*-type crypts (Fig. 1e). These observations strongly suggested that *cd*- and *d*-type crypts might have evolved independently. The SIR of the foci[29] was in fact more than 1.0 for all the stained lesions and tended to be higher in dACF than in cACF, but failed to completely distinguish between the two (Fig. S1), consistent with our previous study.[29] These observations confirmed the relevance of the size of the luminal opening, but not SIR of the foci, for the right diagnosis of dACF.

Dysplasia-associated ACF histologically manifested dysplasia of all grades. Among 71 dACF, vertical sections were successfully prepared for 54 lesions, 45 $cACF^{+ve}$ and 9 $cACF^{-ve}$ (Fig. 2b). Histological analysis revealed that 51 dACF were dysplastic (94%) and 3 hyperplastic (6%). The $cACF^{+ve}$ lesions predominantly comprised moderate dysplasia and $cACF^{-ve}$ severe dysplasia (Fig. 2c). The SIR did not correlate with histological grades (Fig. S2), further declining its relevance. Notably, dysplastic crypts predominantly below the mucosal surface could be detected as dACF (#3–6 of Fig. 2a). Staining with AB-PAS clarified that mucin depletion was exclusively in $cACF^{-ve}$ lesions (Fig. 2d), and accumulation of red granules, indicative of Paneth cell differentiation due to Wnt activation,[31] only in $cACF^{-ve}$ (Fig. 2a and Fig. S3). Accumulation of β-catenin was observed in only a few $cACF^{+ve}$, but in the majority of $cACF^{-ve}$ (Fig. 2e). These findings implied that dACF could manifest dysplasia of all grades, with $cACF^{-ve}$ representing Wnt-activated more advanced lesions than $cACF^{+ve}$. Sequencing analysis of microdissected BCACs from 10 $cACF^{+ve}$ and 10 $cACF^{-ve}$ for *Ctnnb1* mutation identified only one activating mutation from A to G substituting Asp at codon 32 with Asn in a lesion from $cACF^{+ve}$, but not in any

lesion from $cACF^{-ve}$, implying non-genetic mechanisms for AOM-induced β-catenin accumulation, at least in early stages.

Dysplasia-associated ACF overlapped both cACF and advanced preneoplastic lesions. To relate dACF to other known preneoplastic lesions, the colons from three AOM-treated rats were serially stained to detect these lesions, and images of the same foci were directly compared (Fig. 3a). Staining with AB visualized four to five MDF per rat exclusively in the distal colon (Fig. 3b), as previously reported.[9,21] Subsequent brief exposure to MB visualized fACF, which completely coincided with MDF in a total of 14 lesions from three rats (Fig. 3c). By longer exposure to MB and subsequent destaining, 200–300/rat cACF and ~120/rat dACF were visualized (Fig. 3c). Dysplasia-associated ACF tended to be in the more distal colon than cACF, in line with the dysplastic nature of dACF. Approximately 100 and 20 dACF were diagnosed as $cACF^{+ve}$ and $cACF^{-ve}$, respectively (Fig. 3d), consistent with our pilot experiment. Taken together, dACF had a significant overlap with cACF and contained an entire population of MDF and fACF. Representative cases are shown in Figure 4; dACF-1 is $cACF^{+ve}$ (Fig. 4a–e) and dACF-2,3,4 are $cACF^{-ve}$ (Fig. 4f–q). Unlike dACF, all the other lesions were not constantly positive for these four foci. Of note, dACF-2 could be detected only as dACF, strongly suggesting higher sensitivity of dACF for dysplasia.

Scoring dACF enables robust identification of dysplasia. We next wondered, conversely, if the dysplasia could appear as dACF. To address this issue, we thoroughly examined a defined part of the colon, both by histological analysis on horizontal sections, and by serially scoring preneoplastic lesions on the whole mounted colon. We scrutinized segment III of rat #1 (Fig. 5a) because it harbored the highest number of dACF across the samples (Fig. 3c). Of 64 dysplasia, 62 were successfully related between the images of H&E staining and those of the mucosal surface. It was revealed that 56 (90%) and 43 (69%) dysplasia were previously detected as dACF and cACF, respectively, whereas only 4 (6.5%) were diagnosed as fACF/MDF (Fig. 5b, Table S1). Dysplasia-associated ACF and cACF achieved the highest and second highest detection rate, respectively, but 42 of 43 cACF lesions were also detected as dACF, underscoring the superiority of dACF. The detection rates of fACF/MDF, MDC, and BCAC, were comparable to that of cACF only for severe dysplasia (Fig. 5b, Table S1), but still no higher than that of dACF. Representative cases of dysplasia are shown in Figure 5(c). Whereas all the four lesions were diagnosed as dACF, three and two were also diagnosed as BCAC and MDC, respectively. Notably, #58 and #62, identical to dACF-2 and dACF-3 (Fig. 4), respectively, were both diagnosed as MDC, but only #62/dACF-3 was diagnosed as MDF (Fig. 4), clearly indicating that MDF might be less sensitive for dysplasia below the mucosal surface. There was one lesion with severe dysplasia exceptionally undetectable as either dACF or cACF (Table S1). It turned out to be a single aberrant crypt undetectable as MDF despite obvious mucin depletion and β-catenin accumulation (Fig. S4), illustrating the limitation in detecting too small dysplasia as dACF. Taken together, dACF marked with high sensitivity pan-dysplasia of any depth in the mucosa, whereas the other advanced lesions marked dysplasia with modest sensitivity only when on the surface.

Discussion

An ideal marker should be simply detected and easily diagnosed, let alone manifest high specificity and sensitivity. In terms of a marker for dysplasia, however, none of the known preneoplastic lesions of the colon meet all these criteria. As an extension of our previous study, we developed a more straightforward method that enables more specific and sensitive detection of dysplasia in this study. Indeed, 94% of the dACF showed dysplasia, while 90% of the dysplastic lesions proved to be dACF, obviously overwhelming cACF as a marker. Inter-relationships between dACF and various other lesions are summarized in Figure 6.

We developed the new marker by modifying diagnostic steps of the foci. Specifically, we discontinued strict measurement of foci's signal intensity because it proved dispensable and insufficient for detecting and separating dysplastic foci, respectively. Instead, we introduced crypt-based evaluation of the foci for diagnosis of dACF. The crypt subtypes were so distinct that even visual judgment gave concordant results with those obtained by objective quantification. In contrast, we felt that the right diagnosis might be difficult for fACF and MDF, although the visualizing procedure is simple. We were able to spot only relatively large lesions, which resulted in 100% coincident diagnosis of fACF and MDF in our hands, however, examination of the same samples by two experts resulted in a concordant rate as low as 42%,[32] implying difficulties in diagnosing small lesions for non-experts.

The potential of dACF might extend to a marker for tumorigenicity. Currently, incidence of cACF is widely used as a surrogate marker for eventual tumorigenesis based on their high correlation.[7] We showed that the number of dACF is

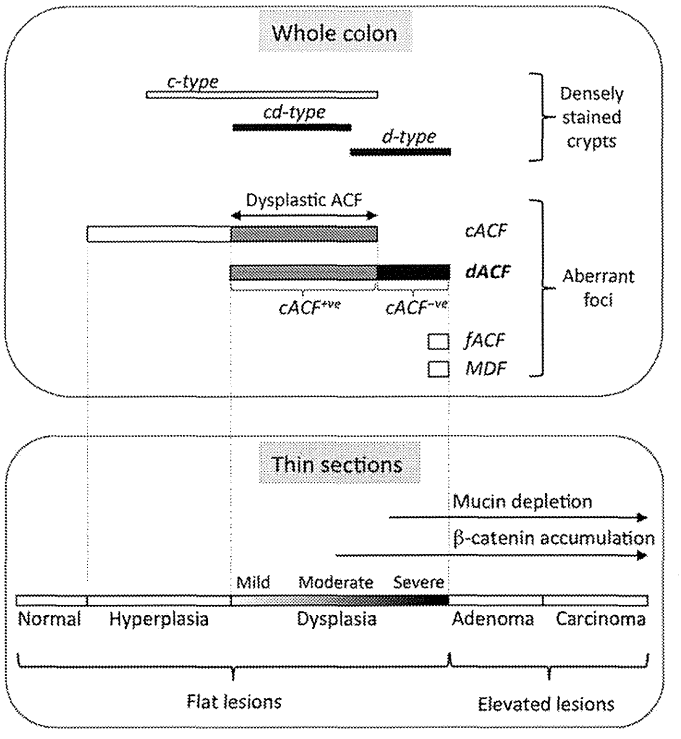

Fig. 6. Dysplasia-associated aberrant crypt foci (dACF) among other preneoplastic lesions of the colon. A summary of the interrelationship between dACF and other preneoplastic lesions, both on unsectioned colon and in thin sections. The spectra of various lesions along multistep colon carcinogenesis clearly indicate that dACF successfully filled in the gap between mucin-depleted foci (MDF)/flat ACF (fACF) and classical ACF (cACF) in detection of dysplasia. *c*-type, enlarged crypt and broad opening; *cd*-type, enlarged crypt and narrow opening; *d*-type, small crypt and narrow opening.

approximately half that of cACF, with a large overlap with the cACF, which is still large enough to yield a proper dynamic range for quantitative evaluation. Given the close association of dACF with dysplasia, it is conceivable that the number of dACF could have more accurately predicted the incidence of eventual tumor development, had it been applied to a case where retinoids decreased the number of cACF, but not that of tumors.[33] It is also tempting to speculate that the relationship between cACF and dACF might account for the long-appreciated correlation between the incidence of cACF and eventual tumorigenesis, presumably through a correlation between the incidence of dACF and dysplasia, justifying the past studies using incidence of cACF as a marker for tumorigenicity.

Crypt-based analysis of dACF also clarified novel aspects of the early stages of colon carcinogenesis. The foci with more than two *d*-type crypts tended not to coexist with *c*-type crypts within the same foci, in line with the previous observation that adenomatous ACF developed from hyperplastic ACF,[34] while it was not the case with *cd*-type crypts. Together with a mutually exclusive relationship within the same foci, *d*- and *cd*-type crypts might constitute a distinct population that follows different pathways toward tumor development. To gain insights into the molecular differences between the two types, we compared $cACF^{-ve}$ and $cACF^{+ve}$ subsets of dACF, which contained exclusively *d*-type and predominantly *cd*-type, respectively. β-catenin accumulation and mucin depletion was significantly more frequent in $cACF^{-ve}$, clearly indicating that $cACF^{-ve}$ are more advanced lesions. However, activating mutation of *Ctnnb1* was rarely found in both subsets, strongly suggesting alternative mechanisms for Wnt activation in early stages, such as *APC* knockdown by *SND1* overexpression.[35] Although *d*- and *cd*-type crypts were stained after decolorization of mucosa, underlying molecular mechanisms are poorly understood. Considering MB's high affinity to an acidic substrate, including phosphate,[36] higher staining intensity might reflect higher amounts of nucleic acids and phosphorylated protein in dysplastic foci. A puzzling feature of *d*-type crypts is that they are invisible before decolorization, although they are supposed to be stained by MB. This observation might be partly due to the fact that *d*-type crypts tend to reside predominantly below the stained normal crypts[22] (Fig. 2a, #3–6; Fig. S3, #7–10; Fig. 4h), consistent with the "bottom-up model" for colon carcinogenesis,[37] thereby requiring complete decolorization of surface mucosa. Taken together, further studies on crypt-based analysis would be warranted to elucidate molecular mechanisms underlying colon carcinogenesis.

In conclusion, we showed that dysplasia could be simply identified on an unsectioned colon as dACF. Based on their unique features, dACF might be established as novel standard preneoplastic lesions of the colon, by complementing or substituting cACF, the current gold standard in this field.

Acknowledgments

We thank Ryoichi Masui and Miho Sasaki for their technical assistance, and Toshio Imai for helpful discussions. We are also grateful to the Central Animal Division in the National Cancer Center Research Institute for their support in animal studies. This work was supported in part by a Grant-in-Aid for Research on Global Health Issues from the Ministry of Health, Labor and Welfare of Japan (201204006) to H.N., a Grant-in-Aid for Cancer Research for the Third Term Comprehensive 10-Year Strategy for Cancer Control from the Ministry of Health, Labor and Welfare of Japan (201220001) to Y.H., and a Grant-in-Aid for Scientific Research C from the Japan Society for the Promotion of Science (18590710) to M.O.

Disclosure Statement

The authors have no conflict of interest.

References

1 Aoki K, Taketo MM. Adenomatous polyposis coli (APC): a multi-functional tumor suppressor gene. *J Cell Sci* 2007; **120**: 3327–35.
2 Levy DB, Smith KJ, Beazer-Barclay Y, Hamilton SR, Vogelstein B, Kinzler KW. Inactivation of both APC alleles in human and mouse tumors. *Cancer Res* 1994; **54**: 5953–8.
3 Sparks AB, Morin PJ, Vogelstein B, Kinzler KW. Mutational analysis of the APC/beta-catenin/Tcf pathway in colorectal cancer. *Cancer Res* 1998; **58**: 1130–4.
4 Kinzler KW, Vogelstein B. Lessons from hereditary colorectal cancer. *Cell* 1996; **87**: 159–70.
5 Bird RP. Observation and quantification of aberrant crypts in the murine colon treated with a colon carcinogen: preliminary findings. *Cancer Lett* 1987; **37**: 147–51.
6 McLellan EA, Bird RP. Aberrant crypts: potential preneoplastic lesions in the murine colon. *Cancer Res* 1988; **48**: 6187–92.
7 Corpet DE, Tache S. Most effective colon cancer chemopreventive agents in rats: a systematic review of aberrant crypt foci and tumor data, ranked by potency. *Nutr Cancer* 2002; **43**: 1–21.
8 Khare S, Chaudhary K, Bissonnette M, Carroll R. Aberrant crypt foci in colon cancer epidemiology. *Methods Mol Biol* 2009; **472**: 373–86.
9 Caderni G, Femia AP, Giannini A *et al.* Identification of mucin-depleted foci in the unsectioned colon of azoxymethane-treated rats: correlation with carcinogenesis. *Cancer Res* 2003; **63**: 2388–92.
10 Paulsen JE, Loberg EM, Olstorn HB, Knutsen H, Steffensen IL, Alexander J. Flat dysplastic aberrant crypt foci are related to tumorigenesis in the colon of azoxymethane-treated rat. *Cancer Res* 2005; **65**: 121–9.
11 Yamashita N, Minamoto T, Ochiai A, Onda M, Esumi H. Frequent and characteristic K-ras activation and absence of p53 protein accumulation in aberrant crypt foci of the colon. *Gastroenterology* 1995; **108**: 434–40.
12 Takahashi M, Wakabayashi K. Gene mutations and altered gene expression in azoxymethane-induced colon carcinogenesis in rodents. *Cancer Sci* 2004; **95**: 475–80.
13 Nucci MR, Robinson CR, Longo P, Campbell P, Hamilton SR. Phenotypic and genotypic characteristics of aberrant crypt foci in human colorectal mucosa. *Hum Pathol* 1997; **28**: 1396–407.
14 Nakagama H, Ochiai M, Ubagai T *et al.* A rat colon cancer model induced by 2-amino-1-methyl-6-phenylimidazo[4,5-*b*]pyridine, PhIP. *Mutat Res* 2002; **506–507**: 137–44.
15 Jen J, Powell SM, Papadopoulos N *et al.* Molecular determinants of dysplasia in colorectal lesions. *Cancer Res* 1994; **54**: 5523–6.
16 Ochiai M, Ushigome M, Fujiwara K *et al.* Characterization of dysplastic aberrant crypt foci in the rat colon induced by 2-amino-1-methyl-6-phenylimidazo[4,5-*b*]pyridine. *Am J Pathol* 2003; **163**: 1607–14.
17 Yamada Y, Mori H. Pre-cancerous lesions for colorectal cancers in rodents: a new concept. *Carcinogenesis* 2003; **24**: 1015–9.
18 Yamada Y, Yoshimi N, Hirose Y *et al.* Sequential analysis of morphological and biological properties of beta-catenin-accumulated crypts, provable premalignant lesions independent of aberrant crypt foci in rat colon carcinogenesis. *Cancer Res* 2001; **61**: 1874–8.
19 Yamada Y, Yoshimi N, Hirose Y *et al.* Frequent beta-catenin gene mutations and accumulations of the protein in the putative preneoplastic lesions lacking macroscopic aberrant crypt foci appearance, in rat colon carcinogenesis. *Cancer Res* 2000; **60**: 3323–7.
20 Paulsen JE, Steffensen IL, Loberg EM, Husoy T, Namork E, Alexander J. Qualitative and quantitative relationship between dysplastic aberrant crypt foci and tumorigenesis in the Min/+ mouse colon. *Cancer Res* 2001; **61**: 5010–5.
21 Yoshimi N, Morioka T, Kinjo T *et al.* Histological and immunohistochemical observations of mucin-depleted foci (MDF) stained with Alcian blue, in rat colon carcinogenesis induced with 1,2-dimethylhydrazine dihydrochloride. *Cancer Sci* 2004; **95**: 792–7.
22 Nakagama H, Nakanishi M, Ochiai M. Modeling human colon cancer in rodents using a food-borne carcinogen, PhIP. *Cancer Sci* 2005; **96**: 627–36.
23 Ochiai M, Nakagama H, Watanabe M, Ishiguro Y, Sugimura T, Nagao M. Efficient method for rapid induction of aberrant crypt foci in rats with 2-amino-1-methyl-6-phenylimidazo[4,5-*b*]pyridine. *Jpn J Cancer Res* 1996; **87**: 1029–33.

24 Creton SK, Zhu H, Gooderham NJ. The cooked meat carcinogen 2-amino-1-methyl-6-phenylimidazo[4,5-*b*]pyridine activates the extracellular signal regulated kinase mitogen-activated protein kinase pathway. *Cancer Res* 2007; **67**: 11455–62.
25 Ubagai T, Ochiai M, Kawamori T *et al.* Efficient induction of rat large intestinal tumors with a new spectrum of mutations by intermittent administration of 2-amino-1-methyl-6-phenylimidazo[4,5-*b*]pyridine in combination with a high fat diet. *Carcinogenesis* 2002; **23**: 197–200.
26 Ishiguro Y, Ochiai M, Sugimura T, Nagao M, Nakagama H. Strain differences of rats in the susceptibility to aberrant crypt foci formation by 2-amino-1-methyl-6-phenylimidazo[4,5-*b*]pyridine: no implication of *Apc* and *Pla2g2a* genetic polymorphisms in differential susceptibility. *Carcinogenesis* 1999; **20**: 1063–8.
27 Fujiwara K, Ochiai M, Ubagai T *et al.* Differential gene expression profiles in colon epithelium of two rat strains with distinct susceptibility to colon carcinogenesis after exposure to PhIP in combination with dietary high fat. *Cancer Sci* 2003; **94**: 672–8.
28 Igarashi M, Hippo Y, Ochiai M, Fukuda H, Nakagama H. AKT is critically involved in cooperation between obesity and the dietary carcinogen amino-1-methyl-6-phenylimidazo [4,5-b] (PhIP) toward colon carcinogenesis in rats. *Biochem Biophys Res Commun* 2014; **443**: 852–7.
29 Ochiai M, Watanabe M, Nakanishi M, Taguchi A, Sugimura T, Nakagama H. Differential staining of dysplastic aberrant crypt foci in the colon facilitates prediction of carcinogenic potentials of chemicals in rats. *Cancer Lett* 2005; **220**: 67–74.
30 Siu IM, Pretlow TG, Amini SB, Pretlow TP. Identification of dysplasia in human colonic aberrant crypt foci. *Am J Pathol* 1997; **150**: 1805–13.
31 Joo M, Shahsafaei A, Odze RD. Paneth cell differentiation in colonic epithelial neoplasms: evidence for the role of the Apc/beta-catenin/Tcf pathway. *Hum Pathol* 2009; **40**: 872–80.
32 Femia AP, Paulsen JE, Dolara P, Alexander J, Caderni G. Correspondence between flat aberrant crypt foci and mucin-depleted foci in rodent colon carcinogenesis. *Anticancer Res* 2008; **28**: 3771–5.
33 Zheng Y, Kramer PM, Lubet RA, Steele VE, Kelloff GJ, Pereira MA. Effect of retinoids on AOM-induced colon cancer in rats: modulation of cell proliferation, apoptosis and aberrant crypt foci. *Carcinogenesis* 1999; **20**: 255–60.
34 Otori K, Sugiyama K, Hasebe T, Fukushima S, Esumi H. Emergence of adenomatous aberrant crypt foci (ACF) from hyperplastic ACF with concomitant increase in cell proliferation. *Cancer Res* 1995; **55**: 4743–6.
35 Tsuchiya N, Ochiai M, Nakashima K, Ubagai T, Sugimura T, Nakagama H. SND1, a component of RNA-induced silencing complex, is up-regulated in human colon cancers and implicated in early stage colon carcinogenesis. *Cancer Res* 2007; **67**: 9568–76.
36 Tong C, Hu Z, Wu J. Interaction between methylene blue and calf thymus deoxyribonucleic acid by spectroscopic technologies. *J Fluoresc* 2010; **20**: 261–7.
37 Boman BM, Fields JZ, Cavanaugh KL, Guetter A, Runquist OA. How dysregulated colonic crypt dynamics cause stem cell overpopulation and initiate colon cancer. *Cancer Res* 2008; **68**: 3304–13.

Supporting Information

Additional supporting information may be found in the online version of this article:

Fig. S1. Signal intensity ratio (SIR) of the foci is insufficient for right diagnosis of dysplasia-associated aberrant crypt foci (dACF). A dot represents each lesion.

Fig. S2. Lack of correlation between histological grade and signal intensity of stained foci.

Fig. S3. Classical aberrant crypt foci $(cACF)^{-ve}$ subset of dysplasia-associated ACF (dACF) manifest severe dysplasia.

Fig. S4. Dysplastic crypt exceptionally undetectable by scoring dysplasia-associated aberrant crypt foci (dACF).

Table S1. Characterization of comprehensively determined dysplastic lesions.

Mutation Research xxx (2013) xxx–xxx

Contents lists available at ScienceDirect
Mutation Research/Genetic Toxicology and Environmental Mutagenesis
journal homepage: www.elsevier.com/locate/gentox
Community address: www.elsevier.com/locate/mutres

In vivo genotoxicity of a novel heterocyclic amine, aminobenzoazepinoquinolinone-derivative (ABAQ), produced by the Maillard reaction between glucose and L-tryptophan

Yukari Totsuka[a,*], Tetsushi Watanabe[b], Souleymane Coulibaly[b], Sae Kobayashi[b], Marina Nishizaki[b], Miho Okazaki[b], Tomohiro Hasei[b], Keiji Wakabayashi[c], Hitoshi Nakagama[a]

[a] Division of Cancer Development System, National Cancer Center Research Institute, Chuo-ku, Tokyo, Japan
[b] Kyoto Pharmaceutical University, 1 Shichono-cho, Misasagi, Yamashina-ku, Kyoto 607-8412, Japan
[c] Graduate Division of Nutritional and Environmental Sciences, University of Shizuoka, Yada, Shizuoka, Japan

ARTICLE INFO

Article history:
Received 1 October 2013
Received in revised form 2 December 2013
Accepted 4 December 2013
Available online xxx

Keywords:
Maillard reaction product
Micronucleated erythrocytes
Comet assay
gpt delta transgenic mice
Diabetes mellitus (DM)

ABSTRACT

We recently demonstrated that a novel heterocyclic amine, 5-amino-6-hydroxy-8*H*-benzo[6,7]azepino[5,4,3-*de*]quinolin-7-one (ABAQ), is produced from glucose and L-tryptophan by the Maillard reaction at physiological temperature and pH, and that ABAQ was strongly mutagenic for *Salmonella* strains in the presence of S9 mix. Here, we present the results of three *in vivo* genotoxicity assays of ABAQ. The comet assay revealed that DNA damage was significantly increased in the livers, kidneys, lungs, and bone marrows of ICR mice, 3 h after i.p. injection of ABAQ (50 mg/kg body weight (bw)). To evaluate clastogenicity, the peripheral blood micronucleus test was performed, also in ICR mice. ABAQ induced micronucleated reticulocytes (MNRETs) in a dose-dependent manner; the frequency of MNRETs was significantly elevated at all i.p. doses (12.5, 25, and 50 mg/kg bw) after 48 h. To investigate the mutagenicity of ABAQ *in vivo*, *gpt* delta transgenic mice were treated with five consecutive administrations of ABAQ by gavage at doses of 25 or 50 mg/kg per week for 3 weeks. The frequencies of *gpt* mutations (MF) in the liver of mice increased significantly compared with controls, in a dose-dependent manner. No significant increase of *gpt* MF was detected in the kidneys. Base substitutions predominated; both G:C → A:T and A:T → C:G mutations were significantly increased by ABAQ. The Spi$^-$ MF was also significantly increased in the liver after ABAQ treatment. If formed *in vivo*, ABAQ may give rise to adverse genotoxic effects.

1. Introduction

Diabetes mellitus (DM) affects more than 300 million people worldwide and the number is predicted to increase to at least 400 million by 2030 [1]. Epidemiological studies show that diabetes patients have an increased incidence of cancers in certain organs, including liver, pancreas, kidney, and endometrium [2–5]; however, the causal mechanisms are not fully elucidated. A consistent increase in blood sugar levels is characteristic of diabetes, and the Maillard reaction is considered to be implicated in diabetic complications [6]. The Maillard reaction comprises a series of complex non-enzymatic reactions between the carbonyl group of a reducing sugar and the amino groups of amino acids, peptides, or proteins to yield an unstable Schiff base, which then leads to a relatively stable ketoamine known as an Amadori product [7]. The Amadori products react with amino acids or are converted into reactive carbonyl species, such as deoxyglucosone. During the latter stage of the reaction, the carbonyl species react with amino groups in proteins and other molecules.

We recently found that the Maillard reaction of glucose and L-tryptophan at physiological temperature and pH (37 °C and pH 7.4) produces mutagens, and we identified a novel heterocyclic amine,

Abbreviations: ABAQ, 5-amino-6-hydroxy-8*H*-benzo[6,7]azepino[5,4,3-*de*]quinolin-7-one; MNRETs, micronucleated reticulocytes; MF, mutation frequencies; DM, diabetes mellitus; PhIP, 2-amino-1-methyl-6-phenylimidazo[4,5-*b*]pyridine; *gpt*, guanine phosphoribosyltransferase; LMP, low melting point; NMP, normal melting point; DMSO, dimethyl sulfoxide; 6-TG, 6-thioguanine; SD, standard deviation; HCAs, heterocyclic amines.

* Corresponding author at: Division of Cancer Development System, National Cancer Center Research Institute, 1-1, Tsukiji 5-chome, Chuo-ku, Tokyo 104-0045, Japan. Tel.: +81 3 3547 52014552; fax: +81 3 3542 2530.
E-mail address: ytotsuka@ncc.go.jp (Y. Totsuka).

1383-5718/$ – see front matter © 2013 Elsevier B.V. All rights reserved.
http://dx.doi.org/10.1016/j.mrgentox.2013.12.002

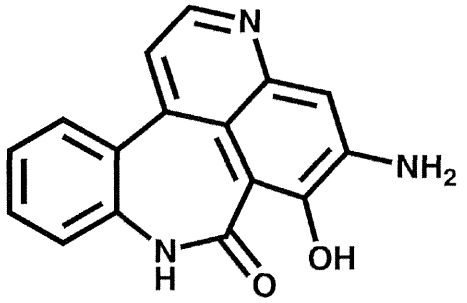

Fig. 1. Chemical structure of 5-amino-6-hydroxy-8*H*-benzo[6,7]azepino[5,4,3-*de*]quinolin-7-one (ABAQ).

5-amino-6-hydroxy-8*H*-benzo[6,7]azepino[5,4,3-*de*]quinolin-7-one (ABAQ, Fig. 1), from the reaction mixture [8]. A plausible mechanism for the formation of ABAQ from glucose and L-tryptophan is also shown in our previous report [8]. ABAQ induced mutations in *Salmonella typhimurium* strains TA98, TA100, YG1024, and YG1029 in the presence of S9 mix, and the mutagenic potency was the highest in YG1024, a derivative of TA98 that overproduces *O*-acetyltransferase. These results suggest that ABAQ mutagenicity depends on metabolic activation catalyzed by cytochrome P450 and *O*-acetyltransferase [8]. These characteristics are very similar to those of a cooked food-derived heterocyclic amine, 2-amino-1-methyl-6-phenylimidazo[4,5-*b*]pyridine (PhIP), suggested to be formed by the reaction of creatine with Maillard reaction products from glucose and phenylalanine by heating at high temperatures [9]. The mutagenic potencies of ABAQ in TA98 and YG1024 are comparable to those of PhIP [8].

Because ABAQ was discovered only recently, its biological activities have not been determined, aside from *Salmonella* mutagenicity. In the present study, therefore, we have examined the genotoxicity of ABAQ *in vivo*, and compared it to that of PhIP; the acute studies used the micronucleus and comet assays; chronic mutagenicity was evaluated using the *gpt* delta transgenic mouse system, in which point mutations and deletions can be assessed by *gpt* and Spi$^-$ selection, respectively [10,11]. We show here that ABAQ induces acute and chronic genotoxicity, and discuss the possible underlying mechanisms.

2. Materials and methods

2.1. Chemicals

ABAQ (more than 99% pure) was obtained from Hamari Chemicals, Ltd. (Osaka, Japan). Corn oil, low melting point (LMP) and normal melting point (NMP) agarose, dimethyl sulfoxide (DMSO), and Triton X-100 were purchased from Sigma–Aldrich (St. Louis, MO, USA). PhIP·HCl and other chemicals were purchased from Wako Pure Chemical Industries (Osaka, Japan).

2.2. Experimental animals

Male ICR mice (6 weeks old) and guanine phosphoribosyltransferase (*gpt*) delta mice (6 weeks old) were purchased from Japan SLC (Shizuoka, Japan). The *gpt* delta mice carry approximately 80 copies of *lambda* EG10 DNA on chromosome 17 on a C57BL/6J background [12]. The animals were provided with food (CE-2 pellet diet; CLEA Japan, Inc., Tokyo, Japan) and tap water *ad libitum*, and maintained under controlled conditions as follows: a 12-h light/dark cycle, 22 ± 2 °C room temperature, and 55 ± 10% relative humidity. After quarantine for one week, the experiments were conducted according to the "Guidelines for Animal Experiments in the National Cancer Center or Kyoto Pharmaceutical University", and the animal studies were approved by its Experimental Animal Research Committee.

2.3. In vivo comet assay

The alkaline comet assay was performed according to a published method [13]. ABAQ was suspended in olive oil and 25, 50, or 100 mg/kg body weight (bw) doses were injected intraperitoneally (i.p.). PhIP was dissolved in physiological saline and administered i.p. to mice at 12.5, 25, or 50 mg/kg bw. Controls received olive oil or physiological saline i.p. Five ICR mice were used for each group. Liver, kidneys, lungs, and bone marrow were removed 3 h after the injections. Each organ, except for bone marrow, was minced, suspended in chilled homogenizing buffer (pH 7.5, 0.075 M KCl and 0.03 M sodium EDTA), and homogenized gently with a Dounce-type homogenizer. Normal melting point agarose (100 μl) was layered as the first layer on a glass slide; LMP agarose (50 μl) containing 1000 nuclei was layered next; normal melting point agarose (100 μl) was layered last. The slides were immersed in ice-cold lysing solution (pH 10, containing 2.5 M NaCl, 100 mM sodium EDTA, 10 mM Tris–HCl, 1% sodium N-lauryl sarcosinate, 10% DMSO and 1% Triton X-100) for 60 min. The slides were placed on a horizontal gel electrophoresis platform and covered with chilled alkaline solution (containing 300 mM NaOH, 1 mM sodium EDTA) for 20 min to allow for the DNA to unwind and expose alkali-labile sites. The nuclei were electrophoresed at 25 V (1 V/cm) for 20 min. After electrophoresis, the specimens were rinsed twice with 400 mM Tris–HCl (pH 7.5) to neutralize excess alkali, stained with 50 μl ethidium bromide solution, and covered with a cover slip. Nuclei (100 per organ per animal) were inspected using a fluorescence microscope equipped with a CCD camera. The tail moment of the DNA was measured using Komet Assay software (Kinetic Imaging Ltd., Liverpool, UK).

2.4. In vivo micronucleus test

The micronucleus test was carried out according to a published method [14]. ABAQ suspended in olive oil or PhIP dissolved in physiological saline were administered i.p. at 12.5, 25, or 50 mg/kg bw. Control mice were treated with either olive oil or physiological saline. Five ICR mice were used for each group. Peripheral blood (5 μl) was obtained from the ventral tail, spread on an acridine orange-coated glass slide, and covered with a cover slip. Supravitally stained reticulocytes were observed using a fluorescence microscope with a blue excitation and a yellow-to-orange barrier filter. The number of MNRETs per 1000 reticulocytes was scored for each mouse.

2.5. gpt and Spi$^-$ mutation assays

For mutation analysis, each group of five male *gpt* delta mice was orally administered five consecutive doses (25 or 50 mg/kg) of ABAQ per week for 3 weeks. The control mice ($n = 4$) were treated with solvent (corn oil) alone. The mice were sacrificed at 14 weeks age (5 weeks after ABAQ administration). Liver and kidneys were removed and stored at −80 °C until high-molecular-weight genomic DNA was extracted using a RecoverEase DNA Isolation Kit (Agilent Technology, USA) according to the manufacturer's instructions. *Lambda* EG10 phages were rescued using Transpack Packaging Extract (Stratagene, La Jolla, CA). The *gpt* and Spi$^-$ mutagenesis assays were performed according to published methods [12]. Briefly, *E. coli* YG6020 was infected with the phage and spread on M9 salt plates containing chloramphenicol (Cm) and 6-thioguanine (6-TG) and incubated for 72 h at 37 °C to select for colonies harboring a plasmid carrying the gene encoding chloramphenicol acetyltransferase, as well as a mutated *gpt*. The

Please cite this article in press as: Y. Totsuka, et al., *In vivo* genotoxicity of a novel heterocyclic amine, aminobenzoazepinoquinolinone-derivative (ABAQ), produced by the Maillard reaction between glucose and L-tryptophan, Mutat. Res.: Genet. Toxicol. Environ. Mutagen. (2013), http://dx.doi.org/10.1016/j.mrgentox.2013.12.002

6-TG-resistant isolates were cultured overnight at 37 °C in LB broth containing 25 mg/mL Cm, harvested by centrifugation (7000 rpm, 10 min), and stored at −80 °C.

The mutational spectra of 6-TG coding sequences were determined using PCR and direct sequencing, and a 739-bp DNA fragment containing *gpt* was amplified by PCR as described previously [12]. Sequence analysis was performed at Takara Bio Inc. (Mie, Japan). The Spi⁻ assay was performed as described previously [11,12]. The lysates of Spi⁻ mutants were obtained by infection of *E. coli* LE392 with the recovered Spi⁻ mutants.

2.6. Statistical analysis

Comet assay and micronucleus test data are expressed as means ± standard deviation (SD). Student's *t*-test was used to evaluate the significance of differences of DNA tail moment in the comet assay and the frequency of MNRETs in the micronucleus test between groups treated with ABAQ, PhIP, and control groups. The data from the *gpt* and Spi⁻ mutation assays were expressed as means ± SD. The data were compared with the corresponding solvent control using the F test before application of the Student's *t*-test. Mutational spectra were compared using Fisher's exact test [15]. *P* values lower than 0.05 were considered to indicate statistical significance.

3. Results

3.1. Analysis of acute DNA-damaging activity of ABAQ and PhIP in multiple organs (in vivo comet assay)

DNA damage induced by ABAQ and PhIP in multiple organs (liver, kidneys, lungs, and bone marrow) was evaluated as the DNA tail moment, 3 h after i.p. administration, using the comet assay under alkaline conditions. As shown in Fig. 2, the DNA tail moment values increased in a dose-dependent manner following ABAQ treatment, and the values for all organs were significantly higher at 50 and 100 mg/kg bw compared with those of control mice. High mean tail moments were detected in the bone marrow of mice treated with 50 and 100 mg/kg bw and DNA damage values were 1.3- and 1.4-fold higher, respectively compared with the control ($P < 0.01$ at both doses). For PhIP, a significant increase of DNA tail moment values was detected in all organs examined at 12.5, 25, and 50 mg/kg bw. The highest tail moment was detected in the kidneys at 50 mg/kg bw and the DNA damage was 1.3-fold ($P < 0.01$) higher than that of the control group.

3.2. Clastogenicity of ABAQ and PhIP in peripheral blood (in vivo micronucleus test)

The clastogenic activities of ABAQ and PhIP were examined by the micronucleus test. Frequencies of MNRETs were increased dose-dependently, 24 h and 48 h after the administration of ABAQ, and the frequencies were significantly elevated at all doses examined (12.5, 25, and 50 mg/kg bw) at 48 h. The highest frequencies of MNRETs were detected at 48 h, and the frequencies were 3.0-, 4.2-, and 5.8-fold higher than controls at 12.5, 25, and 50 mg/kg bw, respectively ($P < 0.01$ at each dose). Similarly, the frequency of MNRETs was dose-dependently increased 24 and 48 h after injection of PhIP, and was the highest at 50 mg/kg bw at 48 h after administration; the value was 7.4-times higher than that of controls ($P < 0.01$) (Fig. 3).

3.3. gpt and Spi⁻ mutations in the liver and kidneys of gpt transgenic mice treated with ABAQ

3.3.1. General observations of gpt delta transgenic mice administrated ABAQ

Body weights of *gpt* delta mice receiving vehicle control reached 27.5 ± 3.1 g, 30 d after gastric intubation. Values for *gpt* delta mice receiving multiple doses of ABAQ at 25 or 50 mg/kg bw were 28.7 ± 2.3 g and 28.5 ± 1.5 g, respectively, 30 d after administration, and no significant difference was observed compared with the vehicle control group. The average dietary consumption per day per mouse was about 3 g and was not affected by ABAQ.

3.3.2. gpt mutations in the liver and kidneys of gpt transgenic mice following ABAQ treatment

To determine the mutagenic effects of ABAQ in the liver and kidneys, *gpt* delta transgenic mice were treated with low or high doses of ABAQ (five consecutive administrations of ABAQ by gavage of 25 or 50 mg/kg bw per week for 3 weeks). Data are summarized in Table 1 and Fig. 4. MFs in the liver induced by both doses of ABAQ were significantly increased, 3.3- or 3.6-fold compared with the vehicle controls (Fig. 4A). In contrast, there was no increase in the MF in the kidneys following the low dose of ABAQ. The high dose of ABAQ resulted in a slight increase in the MF, but it was not statistically significant (Fig. 4B).

PCR and DNA sequence analyses revealed 42 and 14 independent 6-TG-resistant mutations induced by ABAQ and in the vehicle controls, respectively. The classes of *gpt* mutations are summarized in Table 2. Because our control samples were limited, previously

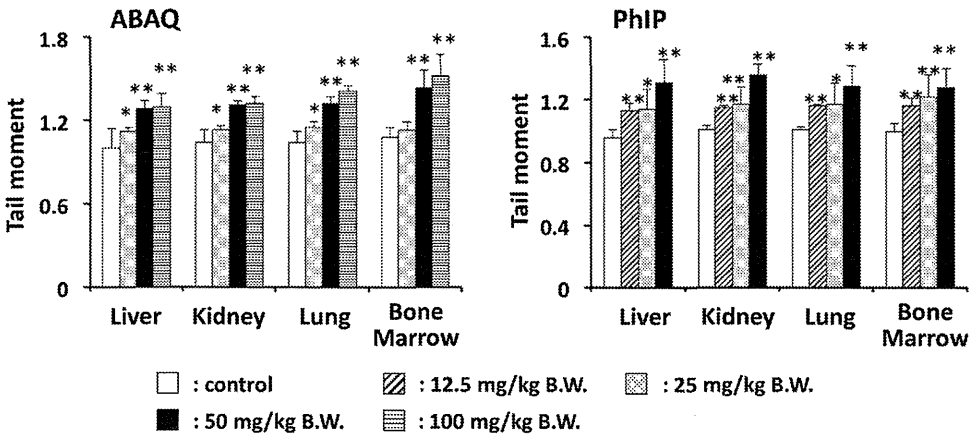

Fig. 2. DNA-damaging activity of ABAQ and PhIP in various organs of mice. Mice were injected i.p. with four doses of either ABAQ or PhIP. Control mice were treated with olive oil or physiological saline. Organs were removed at 3 h after the injection. The values represent the mean of five mice ± SD. Tail moment values of organs untreated mice for ABAQ and PhIP experiments were as follows: liver (1.00 ± 0.14 and 0.96 ± 0.05), kidney (1.04 ± 0.09 and 1.01 ± 0.03), lung (1.04 ± 0.08 and 1.01 ± 0.02), bone marrow (1.08 ± 0.07 and 1.00 ± 0.05). *$P < 0.05$ (*vs.* control), **$P < 0.01$ (*vs.* control).

Please cite this article in press as: Y. Totsuka, et al., *In vivo* genotoxicity of a novel heterocyclic amine, aminobenzoazepinoquinolinone-derivative (ABAQ), produced by the Maillard reaction between glucose and L-tryptophan. Mutat. Res.: Genet. Toxicol. Environ. Mutagen. (2013), http://dx.doi.org/10.1016/j.mrgentox.2013.12.002

Table 1
Summary of *gpt* mutation frequency in the liver and kidneys of *gpt* delta mice treated with ABAQ.

	Mouse ID	Number of colonies		MF ($\times 10^{-6}$)	Average MF ($\times 10^{-6}$)[a]
		Mutant	Total		
Liver					
[b]Control	1	5	907,500	5.51	
	2	5	892,500	5.60	
	3	1	862,500	1.16	
	4	3	627,000	4.78	
	Total	14	3,289,500		4.26 ± 2.10
ABAQ					
25 mg/kg × 5	1	8	361,500	22.13	
	2	1	613,500	1.63	
	3	6	625,500	9.59	
	4	10	453,000	22.08	
	5	7	463,500	15.10	
	Total	32	2,517,000		14.11 ± 8.73*
50 mg/kg × 5	1	14	1,129,500	12.39	
	2	10	978,000	10.22	
	3	14	1,003,500	13.95	
	4	27	1,137,000	23.75	
	5	15	922,500	16.26	
	Total	80	5,170,500		15.32 ± 5.20**
Kidneys					
[b]Control	1	4	709,500	5.64	
	2	4	366,000	10.93	
	3	3	384,000	17.81	
	4	5	361,500	13.83	
	Total	16	1,821,000		9.55 ± 3.58
ABAQ					
25 mg/kg × 5	1	8	928,500	6.46	
	2	5	715,500	6.99	
	3	3	519,000	5.78	
	4	14	991,500	14.12	
	5	9	571,500	15.75	
	Total	37	3,726,000		9.82 ± 4.72
50 mg/kg × 5	1	6	702,000	12.39	
	2	5	985,500	10.22	
	3	7	529,500	13.95	
	4	11	492,000	23.75	
	5	12	657,000	16.26	
	Total	41	3,366,000		13.49 ± 7.01

[a] Mean ± SD.
[b] Solvent control (corn oil).
* $P < 0.05$.
** $P < 0.01$ (*vs.* solvent control) by Student's *t*-test.

Table 2
Classification of *gpt* mutations detected in the liver of control and ABAQ-treated mice.

Type of mutation	Control		Control-2[a]		ABAQ		*P* value[b]
	No. of mutations (%)	Specific MF[c] ($\times 10^{-6}$)	No. of mutations (%)	Specific MF[c] ($\times 10^{-6}$)	No. of mutations (%)	Specific MF[c] ($\times 10^{-6}$)	
Base substitution							
Transition							
G:C to A:T	7(46.7)	2.13	21(42.9)	2.78	14(33.3)	5.77	0.02[d], 0.03[e]
A:T to G:C	0(0)	0.00	4(8.2)	0.53	3(7.1)	1.24	0.04[d], 0.25[e]
Transversion							
G:C to T:A	5(33.3)	1.52	5(10.2)	0.66	9(21.4)	3.71	0.10[d], 0.0005[e]
G:C to C:G	0(0)	0.00	2(4.1)	0.26	1(2.4)	0.41	0.24[d], 0.72[e]
A:T to T:A	0(0)	0.00	4(8.2)	0.53	4(9.5)	1.65	0.02[d], 0.09[e]
A:T to C:G	0(0)	0.00	1(2.0)	0.13	3(7.1)	1.25	0.04[d], 0.02[e]
Insertion	1(6.7)	0.30	1(2.0)	0.13	1(2.4)	0.41	0.83[d], 0.40[e]
Deletion	2(13.3)	0.61	6(12.2)	0.79	5(12.0)	2.06	0.12[d], 0.10[e]
Others	0(0)	0.00	5(10.2)	0.66	2(4.8)	0.82	0.10[d], 0.79[e]
Total	15[f](100)	4.56	49(100)	6.48	42(100)	17.30	0.00001[d], 0.00001[e]

[a] Data are from Masumura et al. [15].
[b] *P* values were determined using Fisher's exact test according to Carr and Gorelick [14].
[c] Specific MFs were calculated by multiplying the total mutation frequency by the ratio of each type of mutation to the total mutation.
[d] ABAQ *vs* control.
[e] ABAQ *vs* control-2.
[f] One animal had two mutations.

Please cite this article in press as: Y. Totsuka, et al., *In vivo* genotoxicity of a novel heterocyclic amine, aminobenzoazepinoquinolinone-derivative (ABAQ), produced by the Maillard reaction between glucose and L-tryptophan, Mutat. Res.: Genet. Toxicol. Environ. Mutagen. (2013), http://dx.doi.org/10.1016/j.mrgentox.2013.12.002

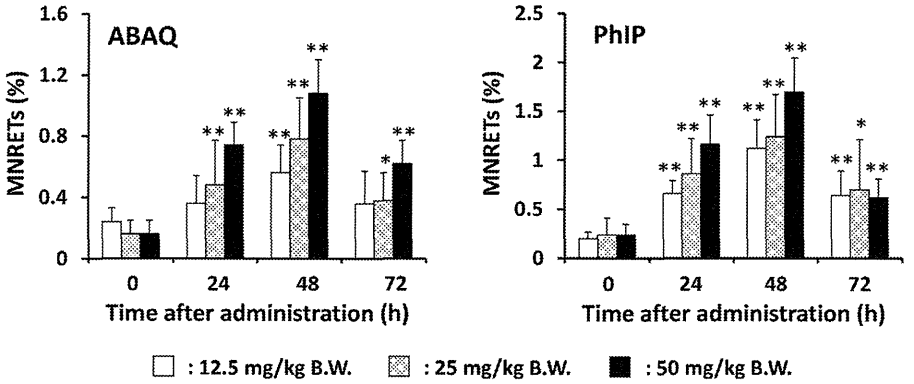

Fig. 3. Clastogenic activity of ABAQ and PhIP in peripheral blood of mice. Mice were injected i.p. with three doses of either ABAQ or PhIP. Control mice were treated with olive oil or physiological saline. One thousand reticulocytes were observed per mouse. The values represent the mean of five mice ± SD. *$P < 0.05$ (*vs.* control), **$P < 0.01$ (*vs.* control).

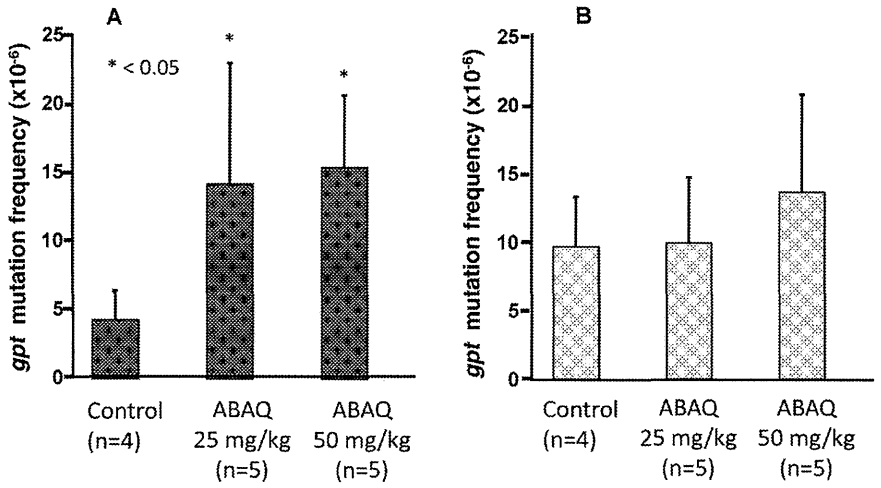

Fig. 4. The *gpt* MFs in the liver (A) and kidneys (B) of mice after multiple administration of ABAQ. Male mice were treated with multiple (25 or 50 mg/kg × 5 times per week for 3 weeks) doses of MGT, and mice were sacrificed 5 weeks after ABAQ administration. The data represent the mean ± SD. *$P < 0.05$, Student's *t*-test *versus* the corresponding vehicle-control mice.

published data [16] are also included in Table 2 (Control-2). Base substitutions predominated in both ABAQ-induced and spontaneous cases. G:C → A:T transitions and A:T → C:G transversions were significantly higher in the ABAQ-treated group.

3.3.3. *Spi⁻ mutations in the liver and kidneys of gpt transgenic mice following ABAQ treatment*

We also measured Spi⁻ MFs in the liver and kidneys of *gpt* delta mice treated with low and high doses of ABAQ (Table 3 and Fig. 5). The mean Spi⁻ MF values in the liver was $1.86 \pm 1.47 \times 10^{-6}$ (control), $6.17 \pm 2.49 \times 10^{-6}$ (low dose) and $6.81 \pm 2.57 \times 10^{-6}$ (high dose), respectively. Spi⁻ MFs in the liver of the both low- and high-dose groups were significantly elevated, up to 2-fold (Fig. 5A). Similar to liver MFs, in the kidneys, Spi⁻ MF showed around 3-fold increase, although this difference was not significant (Fig. 5B).

4. Discussion

The novel heterocyclic amine, ABAQ, identified as a product of the Maillard reaction at physiological temperature and pH, was genotoxic *in vivo*, as revealed by the comet assay, micronucleus test, and *gpt* and Spi⁻ mutation assays. The comet assay is a sensitive method for detecting DNA damages, including double- and single-strand DNA breaks, which are generated indirectly from incomplete excision repair and alkali-labile sites [17]. The DNA tail moment values for liver, kidneys, lungs, and bone marrow in ABAQ-treated (50 mg/kg bw) mice were significantly higher than those of mice treated similarly with PhIP, a representative mutagenic/carcinogenic heterocyclic amine. These results indicate that ABAQ and PhIP have similar levels of DNA-damaging activity in these organs. Under alkaline conditions, not only ABAQ-DNA adducts but also oxidative- and inflammation-related DNA adducts raised by the accompanying immunological response can be measured as DNA damage. ABAQ apparently induced DNA damage in various organs; however, the cause of the damage might be different in each organ. Further studies are required to elucidate this.

The micronucleus test is widely used to detect the clastogenicity of chemicals. Here we show that reticulocytes in the peripheral blood were supravitally stained with acridine orange, and MNRETs can be detected before being trapped and destroyed by the spleen [18]. The frequency of MNRETs was dose-dependently increased at 24 and 48 h after i.p. injection of ABAQ, and the highest frequency was found at 48 h after the injection. Similarly, frequencies of MNRETs increased dose-dependently 24 h and 48 h after PhIP treatment. For ABAQ, the highest frequency of MNRETs was detected 48 h after the injection of 50 mg/kg bw, similar to that observed at 48 h after the injection of 12.5 mg/kg bw PhIP. These results suggest that ABAQ is clastogenic in reticulocytes, with slightly lower potency than that of PhIP.

ABAQ-induced mutations in the liver included base substitutions and deletions. Despite the results of the comet assay, no significant increase of *gpt* and Spi⁻ MF was observed in the kidneys.

Please cite this article in press as: Y. Totsuka, et al., *In vivo* genotoxicity of a novel heterocyclic amine, aminobenzoazepinoquinolinone-derivative (ABAQ), produced by the Maillard reaction between glucose and L-tryptophan, Mutat. Res.: Genet. Toxicol. Environ. Mutagen. (2013), http://dx.doi.org/10.1016/j.mrgentox.2013.12.002

Table 3
Summary of Spi⁻ mutant frequency in the liver and kidneys of *gpt* delta mice treated with ABAQ.

	Mouse ID	Number of colonies		MF ($\times 10^{-6}$)	Average MF ($\times 10^{-6}$)[a]
		Mutant	Total		
Liver					
[b]Control	1	9	2,281,500	5.51	
	2	2	2,767,500	5.60	
	3	3	3,115,500	1.16	
	4	7	3,898,500	4.78	
	Total	21	12,063,000		1.86 ± 1.47
ABAQ					
25 mg/kg × 5	1	9	1,135,500	7.93	
	2	6	1,587,000	3.78	
	3	4	1,267,500	3.16	
	4	8	1,041,000	7.68	
	5	11	1,324,500	8.31	
	Total	38	6,355,500		6.17 ± 2.49**
50 mg/kg × 5	1	12	1,299,000	9.24	
	2	8	804,000	9.95	
	3	7	1,293,500	5.41	
	4	5	1,102,500	4.54	
	5	4	811,500	4.93	
	Total	36	5,310,500		6.81 ± 2.57**
Kidneys					
[b]Control	1	3	1,306,500	2.29	
	2	1	745,500	1.34	
	3	0	763,500	0.00	
	4	1	960,000	1.04	
	Total	5	3,775,500		1.17 ± 0.94
ABAQ					
25 mg/kg × 5	1	0	1,945,500	0.00	
	2	1	1,405,500	0.71	
	3	0	1,048,500	0.00	
	4	2	1,501,500	1.33	
	5	2	1,029,000	1.94	
	Total	5	6,930,000		0.80 ± 0.84
50 mg/kg × 5	1	4	867,000	4.61	
	2	1	1,017,000	0.98	
	3	2	700,500	2.86	
	4	5	790,500	6.33	
	5	1	933,000	1.07	
	Total	13	3,366,000		3.17 ± 1.72

[a] Mean ± SD.
[b] Solvent control (corn oil).
** $P < 0.01$ (*vs.* solvent control), Student's *t*-test.

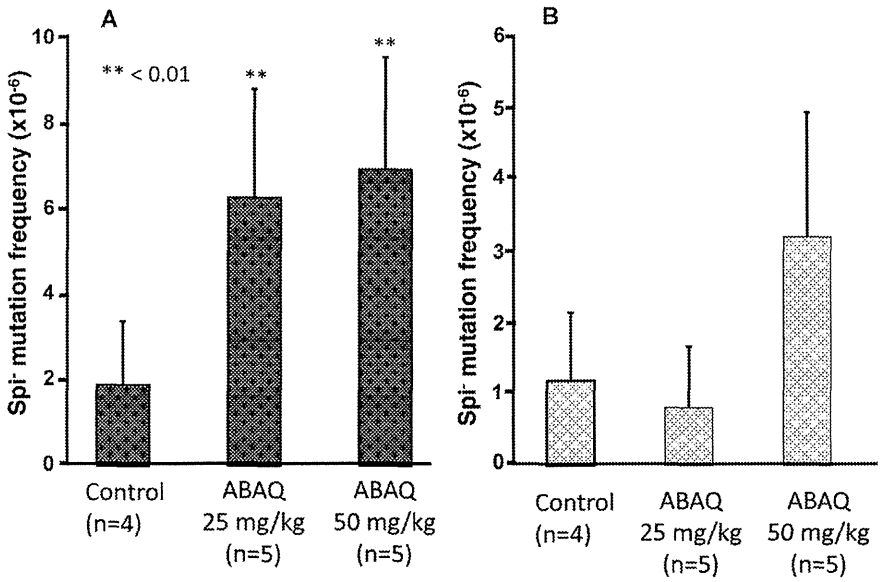

Fig. 5. The Spi⁻ MFs in the liver (A) and kidneys (B) of *gpt* delta mice exposed to multiple doses of ABAQ. An asterisk (*) denotes $P < 0.05$, Student's *t*-test for MFs of ABAQ-treated compared with the corresponding vehicle-control mice.

Please cite this article in press as: Y. Totsuka, et al., *In vivo* genotoxicity of a novel heterocyclic amine, aminobenzoazepinoquinolinone-derivative (ABAQ), produced by the Maillard reaction between glucose and L-tryptophan, Mutat. Res.: Genet. Toxicol. Environ. Mutagen. (2013), http://dx.doi.org/10.1016/j.mrgentox.2013.12.002